科学通报 2020 年 第 65 卷 第 15 期: 1411 ~ 1419
专题: 声学超材料前沿与应用 论 文
《中国科学》杂志社 SCIENCE CHINA PRESS

三维声学超材料的高阶拓扑态

范海燕, 夏百战*

湖南大学机械与运载工程学院, 汽车车身先进设计制造国家重点实验室, 长沙 410082

* 联系人, E-mail: xiabz2013@hnu.edu.cn

2019-10-14 收稿, 2019-12-03 修回, 2019-12-04 接受, 2019-12-04 网络版发表
国家自然科学基金(51621004)资助

摘要 位于“边缘的边缘”上的高阶拓扑态的发现为限制和控制光波、声波以及弹性波的传输提供了一种新思路. 目前, 高阶拓扑态已在二维的机械、电磁、光学、声学和弹性系统中得以实现. 然而, 三维声学系统中对高阶拓扑态的研究却鲜有报道. 本研究针对这一现象提出了一种具有一阶表面态和二阶铰链态的三维声学超材料. 该三维声学超材料可以在其布里渊区的K-H方向上形成二重简并的交线. 改变超材料单胞内外耦合强度的相对大小, 线性简并交线打开形成完全带隙, 生成平庸型和拓扑非平庸型声学超材料. 能带结构、特征频率及传输效率的分析结果表明, 当内耦合强度小于外耦合强度时, 带隙范围内声学超材料具有拓扑非平庸的一阶表面态和二阶铰链态; 当内耦合强度大于外耦合强度时, 带隙范围内声波将无法在声学超材料的任何部位传播, 该声学超材料是平庸的. 三维声学超材料高阶拓扑态的实现突破了二维系统的局限, 在声波能量回收和高精度声传感器方面具有潜在应用前景.

关键词 三维声学超材料, 高阶拓扑绝缘体, 拓扑表面态, 拓扑铰链态, 能带结构

声学超材料具有许多奇特新颖的物理现象, 如强反射、超透射、声隐身、负折射、拓扑态等. 其中近期发现的声学超材料的拓扑态引发研究人员进行了许多有趣的研究[1~3]. 物质的拓扑相位首先是在电子系统中被发现的, 这一发现极大地拓展了我们对凝聚态物理的理解. 如今, 拓扑相位已经扩展到了经典波系统, 包括光学和电磁系统[4,5]以及声学和弹性系统[6~8]. 研究人员先后通过施加外部磁场[9~11]、动态调控系统参数[12,13]、使用光双各向异性材料(optical bianisotropic metamaterial)[14~16]以及利用共振耦合(resonant coupling)[17~19]等方法将拓扑态现象扩展到光子系统, 探讨出了新的拓扑态机理, 并取得了优异的效果. 光子系统中的电磁波可以对磁场进行响应, 但是声子系统中的声波和弹性波却无法响应于磁场. 所以, 对于声子系统, 研究人员又通过陀螺的旋转运动[20~22]、空气的循环流动[23,24]、共振耦合[25,26]和时空调制(spatiotemporal modulation)[27]等方法获得了受拓扑保护的稳健边缘态. 二维拓扑绝缘体的关键特性是具有受拓扑保护的一维无带隙的边缘态, 缺陷和扰动无法阻止边缘态的传输.

若将二维的声子晶体或光子晶体在z方向上周期性叠加, 即可得到三维的晶体结构. 如今, 三维声子晶体和光子晶体中的拓扑态现象主要包括三维拓扑绝缘体[28,29]和三维拓扑半金属[30~32]. 其中, 三维拓扑绝缘体是通过将三维狄拉克点(Dirac point)打开形成带隙, 并且产生受拓扑保护的表面态. 三维拓扑半金属可以实现外尔点(Weyl point)和类似电子外尔半金属中的费米弧(Fermi arcs).

高阶拓扑绝缘体(higher-order topological insulator)是拓扑绝缘体的一种新类别, 这一概念最早是在量化电子系统(quantized electronic systems)中从理论上被提出的[33~36]. 高阶拓扑绝缘体的相位以体极化(bulk polarizations)为特征, 而不以整数拓扑不变量(integer to-

引用格式: 范海燕, 夏百战. 三维声学超材料的高阶拓扑态. 科学通报, 2020, 65: 1411–1419
Fan H Y, Xia B Z. Higher-order topological states in a three-dimensional acoustic metamaterial (in Chinese). Chin Sci Bull, 2020, 65: 1411–1419, doi: 10.1360/TB-2019-0631

© 2019《中国科学》杂志社

pological invariants)为特征，这与传统的拓扑绝缘体[37,38]有所不同. 二维的高阶拓扑绝缘体不存在一维的无带隙边缘态，但是存在零维的位于“边缘的边缘”上的拓扑态, 也就是角态(corner state). 目前, 二维高阶拓扑绝缘体已经在机械[39]、电磁[40]、光学[41]、声学[42~44]和弹性系统[45]中从试验上得到验证. 三维结构可以增大拓扑超材料设计的可能性，但是对三维结构中高阶拓扑态的探究却鲜有报道. 因此, 本研究以二维高阶拓扑绝缘体为基础，设计了具有一阶表面态和二阶铰链态的三维声学拓扑超材料. 首先, 让其原胞能带在布里渊区的K-H方向上形成二重简并的交线. 然后, 改变内外耦合强度的相对大小，打开交线形成完全带隙. 最后, 在拓扑非平庸型带隙内实现受拓扑保护的一阶表面态和二维铰链态.

1 三维声学超材料的几何模型和原胞能带

1.1 三维声学超材料的几何结构

图1(a)表示具有高阶拓扑态的三维声学超材料的整体结构. 该超材料具有三维周期性晶体结构, 其原胞以六角晶格形式在xy平面内进行周期性排列并沿z轴叠加. 图1(b)为声学超材料原胞的几何结构, 其中, 晶格常数为a=97.2 mm. 原胞具有3个充满空气的圆柱, 圆柱直径d=36 mm，高度H=36.9 mm，位于圆柱上下的小空气柱的直径d_3=3.744 mm，高度h=6.3 mm. 相邻圆柱间的耦合由位于H/4处的横向连接空气管道提供. 所有空气柱和空气管道的表面都为硬声场边界.

1.2 理论分析

由于该声学超材料只考虑最近邻耦合(nearest-neighbor couplings)，所以可以运用紧束缚模型(tight-binding model)来分析该结构的性质. 最近邻耦合中的耦合强度可通过改变连接管道的半径来调节. 其中, 内耦合强度t_1与原胞内部空气柱间的连接管道直径d_1的大小成正比, 外耦合强度t_2与原胞内部与外部空气柱间的连接管道直径d_2的大小成正比. 这一紧束缚模型是一维SSH模型[46]的延伸，它的体拓扑(bulk topology)是以体极化(bulk polarizations)为特征的[47], 表述为

$$P_i = -\frac{1}{S}\iint A_i \mathrm{d}^2k, \tag{1}$$

其中, d^2k表示布里渊区的面积元素; $A_i = -i\langle u|\partial k_i|u\rangle$表示最低能带的贝利联络(Berry connection); i=x, y和u, 来自布洛赫函数(Bloch functions); S表示第一布里渊区的面积.

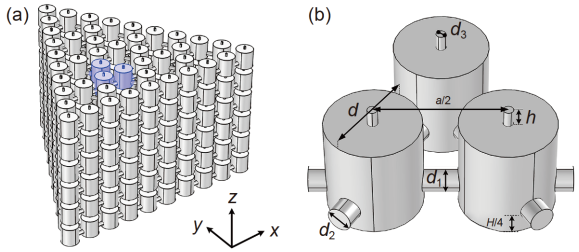


图 1 (网络版彩色)三维声学超材料的几何结构示意图. (a) 整体结构; (b) 原胞的几何结构

Figure 1 (Color online) Schematic diagram of the three-dimensional acoustic metamaterial. (a) The overall structure; (b) geometric structure of the unit cell

因为该声学超材料具有镜像对称性，所以体极化(P_x, P_y)会由于不同数值的t_1和t_2而被限制在两个特定位置上，分别对应于平庸和拓扑非平庸的结构[3,34]. 我们用两个具有代表性的例子来说明体极化(P_x, P_y)的位置. 当d_1=14.976 mm, d_2=3.744 mm时, t_1>t_2, 体极化(P_x, P_y)位于图1(b)中原胞的中心，坐标为(0, 0). 将d_1与d_2的数值互换, 使得t_1<t_2, 则体极化(P_x, P_y)将离开原胞中心, 位置坐标为$(-1/2, -1/2\sqrt{3})$. 根据体边界对应原则[44], 当体极化非零时, 一系列边界模式(如表面态、铰链态等)将出现在结构相应的位置; 当体极化为零时, 将没有任何的边界模式.

1.3 原胞的能带结构

当连接管道的直径d_1=d_2=9.36 mm时，内耦合强度与外耦合强度相等，即t_1=t_2，原胞的能带结构如图2(a)所示. 因为在任一固定数值的k_z下，能带在二维第一布里渊区的角点K与K′点都形成二重简并的单狄拉克点, 所以单狄拉克点沿K-H方向上形成二重简并的交线, 如图2(a)中虚线框所示. 当连接管道的直径d_1=3.744 mm, d_2=14.976 mm时, 内耦合强度小于外耦合强度, 即t_1<t_2, 原胞的能带结构如图2(b)所示. 原本由单狄拉克点构成的K-H方向上交线被打开，形成了频率范围为4505~4721 Hz的完全带隙. 圆点表示被打开的交线在布里渊区的H点(图2(d))上所对应的频率分别为4460和4720 Hz. 将d_1与d_2的数值互换，使t_1>t_2，原胞的能带结构依旧不变. 图2(c)的左部表示d_1=3.744 mm, d_2=14.976 mm时布里渊区的H点所对应的声压场分布; 右部表示d_1=14.976 mm, d_2=3.744 mm时H点的声压场分布. 可

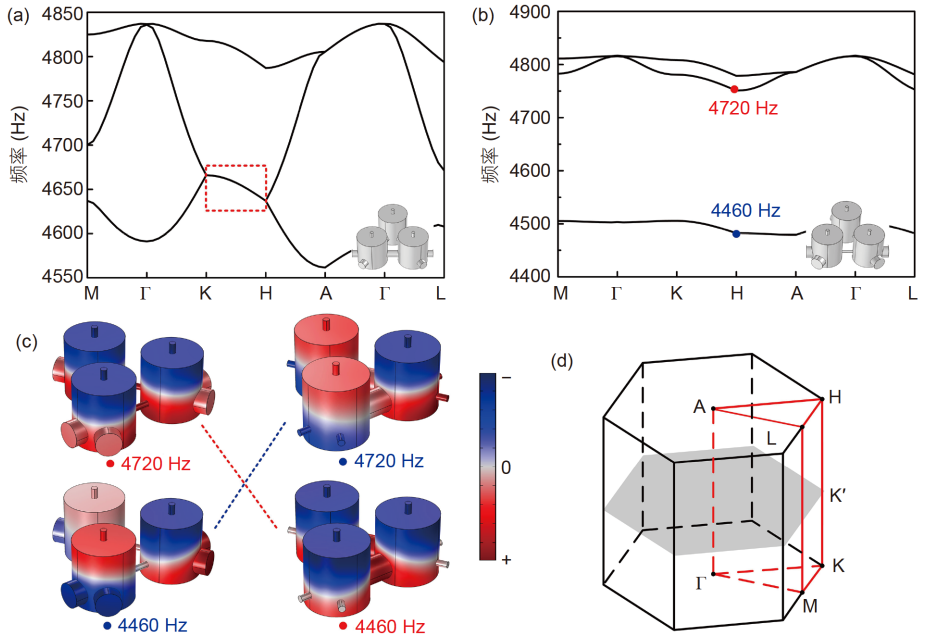


图 2 (网络版彩色)三维声学超材料的原胞能带结构图. (a) 当d_1=d_2=9.36 mm时, 原胞能带结构在K-H方向上形成二重简并的交线(右下角插图为对应的原胞几何结构图); (b) 当 d_1=3.744 mm, d_2=14.976 mm时, 原胞能带结构的交线被打开, 形成完全带隙(插图为对应的原胞几何结构图); (c) d_1=3.744 mm, d_2=14.976 mm和d_1=14.976 mm, d_2=3.744 mm两种情况下, 布里渊区中H点对应的声压场分布; (d) 原胞的第一布里渊区的一半

Figure 2 (Color online) Band structure of the unit cell of the three-dimensional acoustic metamaterial. (a) Band structures of the unit cell with d_1=d_2=9.36 mm. A two-fold nodal line along the K-H direction is formed (the geometric structure of the corresponding unit cell is inserted in the lower right corner); (b) band structures of the unit cell with d_1=3.744 mm, d_2=14.976 mm. The two-fold nodal line is lifted, yielding a complete bandgap (the geometric structure of the corresponding unit cell is inserted in the lower right corner); (c) the sound pressure fields of these two cases with d_1=3.744 mm, d_2=14.976 mm and d_1=14.976 mm, d_2=3.744 mm at the H point of the first Brillouin zone; (d) the schematic for one-half of the first Brillouin zone

以看出, 左部原本位于4460 Hz(4720 Hz)的低频(高频)模态反转到了右部位于4720 Hz(4460 Hz)的高频(低频)模态, 表明能带反转(band inversion)现象的发生. 其实, 不止H点, K-H方向上的任何一点都具有模态反转现象. 图2(d)表示原胞的第一布里渊区, 其中K′处的平面正六边形表示固定数值的k_z的二维第一布里渊区, 直角三角柱表示三维不可约布里渊区.

2 三维声学超材料的超胞能带分析

为了研究三维声学超材料的一阶表面态和二阶铰链态, 本研究构建了三维声学超材料的超胞结构. 超胞由d_1=3.744 mm, d_2=14.976 mm的原胞(t_1<t_2)以六角晶格形式在xy平面内排列而成的正三角形构成(最外部的链接管道被去除), 正三角形的边长为5a, 如图3(c), (d)所示. 将Floquet周期性边界条件施加在超胞的上下表面, 其余边界都为硬声场边界, 超胞的能带结构如图3(a)所示. 在频率范围为4505~4721 Hz的完全带隙中, 出现了12条一阶表面能带(虚线所示)和三条二阶铰链能带(实线所示). 一阶表面能带所对应的频率范围为4541~4605 Hz, 该频率范围下声波能量高度集中于三维声学超材料的表面. 图3(c)为一阶表面能带中k_z=8.5(圆点所示)时声压场的分布情况, 观察可得声波能量高度集中在声学超材料超胞的三条边缘, 然而超胞的体内和角点处几乎没有能量分布. 二阶铰链能带所对应的频率范围为4637~4703 Hz, 该频率范围下声波能量高度集中于声学超材料的三条铰链. 图3(d)为二阶铰链能带中k_z=8.5(圆点所示)时声压场的分布情况, 同样可以观察到声波能量高度集中在声学超材料超胞的角点空气柱中, 而超胞的体内和三条边缘处几乎没有能量分布. 上下体能带所对应的频率范围内, 声波可在声学超材料体内传播.

将d_1与d_2的数值互换, 使得t_1>t_2, 按照同样的方式构建超胞, 得到的超胞能带结构如图3(b)所示. 该能带结构中只存在被完全带隙分隔开的体能带, 不存在任何表面能带或铰链能带. 在完全带隙的频率范围内, 声波传播将被完全阻隔, 无法在声学超材料的任何部位传播. 这一现象表明, 由t_1>t_2的原胞构成的声学超材料是平庸的.

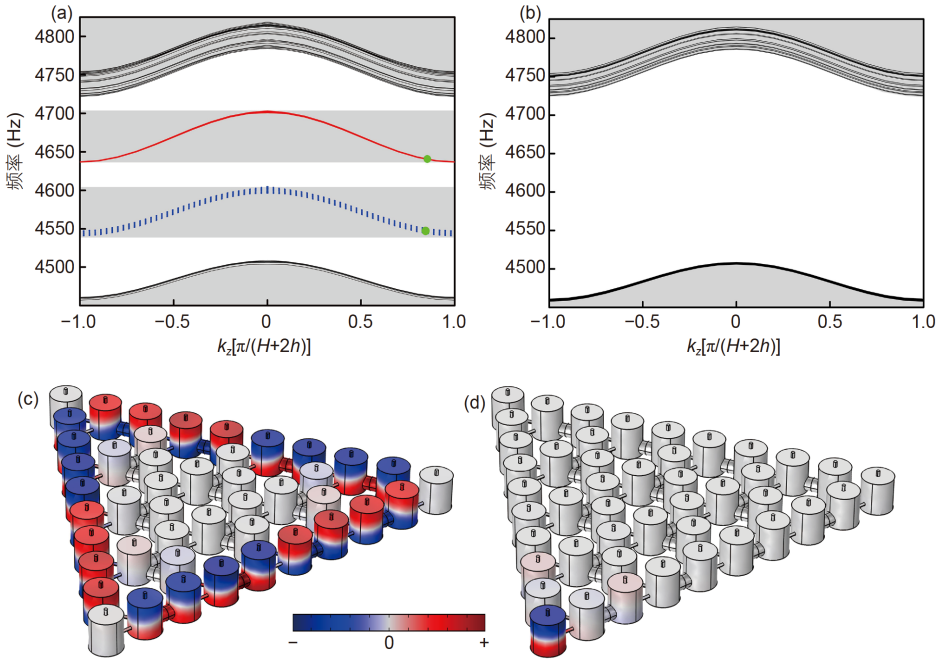


图 3 (网络版彩色)三维声学超材料的超胞能带与声压场分布图. (a) 当$t_1<t_2$时, 超胞的能带结构. 虚线表示一阶表面能带, 实线表示二阶铰链能带; (b) 当$t_1>t_2$时, 超胞的能带结构; (c) 一阶表面能带结构中圆点的声压场分布; (d) 二阶铰链能带结构中圆点的声压场

Figure 3 (Color online) Band structure and acoustic pressure distributions of the supercell of the three-dimensional acoustic metamaterial. (a) Band structure of the supercell with $t_1<t_2$. Solid and dotted lines denote second-order hinge bands and first-order surface bands, respectively; (b) band structure of the supercell with $t_1>t_2$; (c) the acoustic pressure distribution of the round dot in the first-order surface bands; (d) the acoustic pressure distribution of the round dot in the second-order hinge bands

3 三维声学超材料拓扑态的特征频率

3.1 无缺陷结构的特征频率

由60个d_1=3.744 mm和d_2=14.976 mm的原胞($t_1<t_2$)构成的三维声学超材料的整体结构如图4(c)~(f)所示. 图4(a)表示该声学超材料的特征频率. 可以看出, 在完全带隙的频率范围内出现了72个一阶表面特征频率(虚线框所示)和18个二阶铰链特征频率(实线框所示). 一阶表面特征频率的频率范围为4541~4599 Hz, 与超胞计算出的表面能带的频率范围基本一致. 二阶铰链特征频率的范围为4637~4697 Hz, 与超胞计算出的铰链能带匹配较好. 剩余圆点表示体态特征频率, 分为频率大于4721 Hz高频体态特征频率和频率小于4505 Hz低频体态特征频率. 从72个一阶表面特征模态中选取特征频率为4569.1 Hz的特征模态, 如图4(c)所示, 从其声压场的分布情况可以看出声波能量高度集中在声学超材料的表面, 而体内和3条铰链处分布的能量几乎为0. 图4(d)为18个二阶铰链特征模态中特征频率为4669.2 Hz的特征模态, 其声压场分布图表明声波能量高度集中于声学超材料的一条铰链空气柱. 这18个二阶铰链特征频率可以分为6组(如图4(a)中实线框所示), 每组具有3个特征频率相同的特征模态, 每组的3个特征模态中声波能量分别集中在3条铰链空气柱中. 图4(e)表示特征频率为4495.2 Hz的低频体态特征模态, 可以看出它的声波能量高度集中在声学超材料的体内, 巧妙避开了声学超材料的表面和铰链. 图4(f)表示特征频率为4723.2 Hz的高频体态特征模态, 可以发现其声波能量在声学超材料的表面、体内和铰链中都有所分布.

若用60个d_1=14.976 mm和d_2=3.744 mm的原胞($t_1>t_2$)构建三维声学超材料的整体结构, 其特征频率的分布如图4(b)所示. 该图表明$t_1>t_2$的三维声学超材料只具有体态特征频率, 其完全带隙的频率范围内不存在任何表面和铰链特征频率. 这一现象进一步证明, 由$t_1>t_2$原胞构成的声学超材料是平庸的, 而由$t_1<t_2$原胞构成的声学超材料是拓扑非平庸的.

3.2 有缺陷结构的特征频率

为了证明拓扑非平庸的结构中出现的一阶表面态和二阶铰链态是受拓扑保护的, 我们避开了完整结构

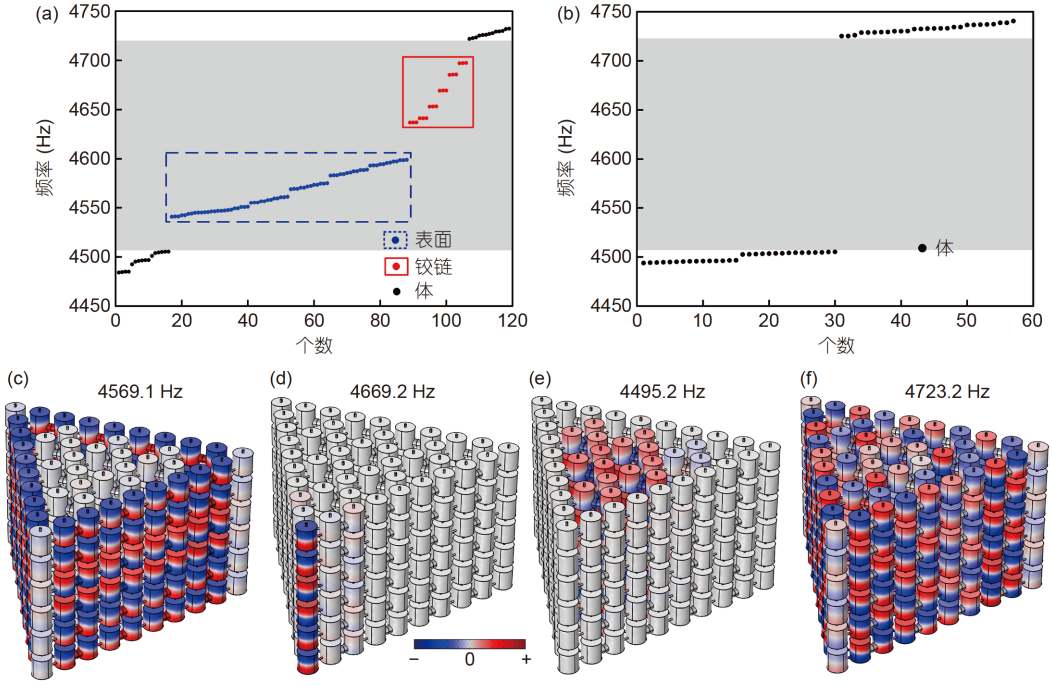


图 4 (网络版彩色)三维声学超材料的特征频率与声压场分布图. (a) 当t_1<t_2时, 整体结构的特征频率分布情况. 其中虚线框内表示一阶表面特征频率, 实线框内表示二阶铰链特征频率, 其余圆点表示体特征频率; (b) 当t_1>t_2时, 整体结构的特征频率分布情况. 圆点表示体特征频率; (c) 特征频率为4569.1 Hz时对应的一阶表面特征模态的声压场分布图; (d) 特征频率为4669.2 Hz时对应的二阶铰链特征模态的声压场分布图; (e) 特征频率为4495.2 Hz时对应的低频体特征模态的声压场分布图; (f) 特征频率为4723.2 Hz时对应的高频体特征模态的声压场分布图

Figure 4 (Color online) Eigenfrequencies and acoustic pressure distributions of the three-dimensional acoustic metamaterials. (a) Numerically evaluated eigenfrequencies of three-dimensional acoustic metamaterial with t_1<t_2. Dots in the solid line box denote second-order hinge eigenfrequencies, dots in the dotted line box denote first-order surface eigenfrequencies, rest dots denote bulk eigenfrequencies. (b) Numerically evaluated eigenfrequencies of three-dimensional acoustic metamaterial with t_1>t_2. Bulk eigenfrequencies are denoted by round dots. (c)–(f) Simulated acoustic pressure distribution of surface eigenfrequency (4569.1 Hz), hinge eigenfrequency (4669.2 Hz), lower frequency bulk eigenfrequency (4495.5 Hz), higher frequency bulk eigenfrequency (4723.2 Hz)

的表面和铰链处, 在完整结构的体内圆柱中插入了一系列缺陷. 缺陷是由半径r=5.4 mm, 高度b=7 mm的金属圆柱构成的, 它们被放置在体内圆柱的底部, 如图5(a)所示. 图5(b)表示完整结构的体内圆柱中任意插入36个金属圆柱后, 具有缺陷结构的特征频率. 可以看出一阶表面态和二阶铰链态的特征频率几乎没有发生改变, 只是完全带隙频率范围略有减小. 这一现象表明这里的一阶表面态和二阶铰链态可以对适度的缺陷免疫, 体现了它们的鲁棒特性.

4 三维声学超材料拓扑态的传输效率

4.1 拓扑非平庸型声学超材料的传输效率

在由60个d_1=3.744 mm和d_2=14.976 mm的原胞(t_1<t_2)构成的三维声学超材料中, 我们在图6(b)所示的1号空气柱施加点声源激励, 并在图6(b)所示的2号空气柱中检测输出声压级, 得到一阶表面态的传输效率曲线如图6(a)中虚线所示. 从该曲线可以看出, 在一阶表面能带频率范围内(图中左部阴影部分), 传输效率较高. 此外, 频率大于4721 Hz时表面态的传输效率高于频率小于4505 Hz时表面态的传输效率. 这是因为在本文提出的拓扑非平庸型声学超材料中, 特征模态的计算结果表明, 频率大于4721 Hz时声波能量不仅集中在声学超材料的体内而且占据了表面, 而频率小于4505 Hz时声波能量只集中在声学超材料的体内(图4(e)~(f)). 所以, 频率大于4721 Hz时的表面传输效率高于频率小于4505 Hz时的表面传输效率. 图6(b)表示在频率为4574 Hz(一阶表面能带频率范围内)的点声源的激励下, 三维声学超材料的声压场分布. 结果显示声波只集中在声学超材料的表面. 我们在图6(c)所示的3号空气柱中施加点声源激励, 并在图6(c)所示的4号空气柱检测输出声压级, 得到二阶铰链态的传输效率曲线如图6(a)中的实线所示. 从该曲线可以看出, 在二阶铰链能带频率范围内(图中右部阴影部分), 其传输效率高

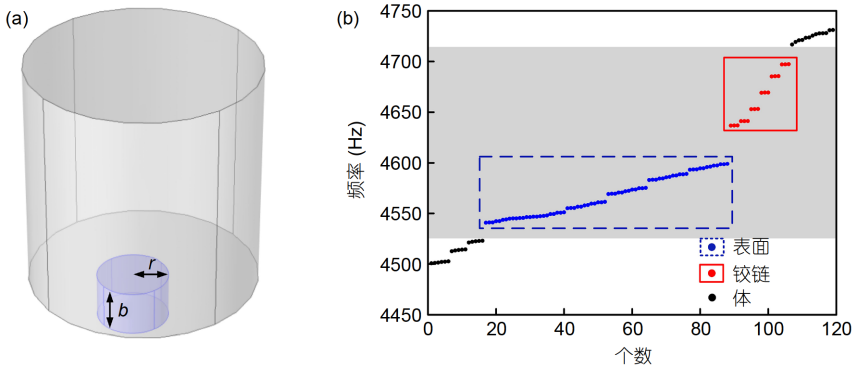


图 5 (网络版彩色)缺陷结构(a)及其特征频率(b). 其中虚线框内表示一阶表面特征频率, 实线框内表示二阶铰链特征频率, 其余圆点表示体特征频率

Figure 5 (Color online) The defect structure (a) and numerically evaluated eigenfrequencies of three-dimensional acoustic metamaterial with defect (b). Dots in the solid line box denote second-order hinge eigenfrequencies, dots in the dotted line box denote first-order surface eigenfrequencies, and rest dots denote bulk eigenfrequencies

于其他频率范围. 而在一阶表面能带频率范围内(图中左部阴影部分), 传输效率具有一个次峰值. 这是因为点声源激励施加在3号空气柱中, 声波为了到达表面会有小部分分配到铰链上, 所以左部阴影部分频率下, 铰链上的传输效率相对于其左右带隙范围内有所上升. 在频率为4670 Hz(二阶铰链能带频率范围内)的点声源的激励下, 三维声学超材料的声压场分布结果如图6(c)所示. 从图中可以看出声波只集中在声学超材料的铰链. 所以, 拓扑非平庸型声学超材料的传输效率的计算结果与其超胞能带和特征频率的计算结果拟合较好.

4.2 平庸型声学超材料的传输效率

在由60个d_1=14.976 mm和d_2=3.744 mm的原胞(t_1>t_2)构成的三维声学超材料中, 在图7(b)所示的1号空气柱中施加点声源激励, 并在图7(b)所示的2号空气柱中检测输出声压级, 得到表面态的传输效率曲线如图7(a)中虚线所示. 按照同样的方法, 在图7(c)所示的3号空气柱中施加点声源激励, 并在图7(c)所示的4号空气柱检测输出声压级, 得到铰链态的传输效率曲线如图7(a)中的实线所示. 从两条曲线可以看出, 在完全带隙的频率范围内(图中阴影部分所示)传输效率都大幅度降低. 因为测量表面态传输效率(虚线)的检测点与激励点的距离较铰链态(实线)的远了许多, 所以表面态的传输效率更低些. 图7(b)表示在频率为4576 Hz (拓扑非平庸型声学超材料的表面能带频率范围内)的点声源的激励下, 三维声学超材料的声压场分布. 图7(c)表示在频率为4652 Hz(拓扑非平庸型声学超材料的铰链能带频率范围内)的点声源的激励下, 三维声学超材料的声压场

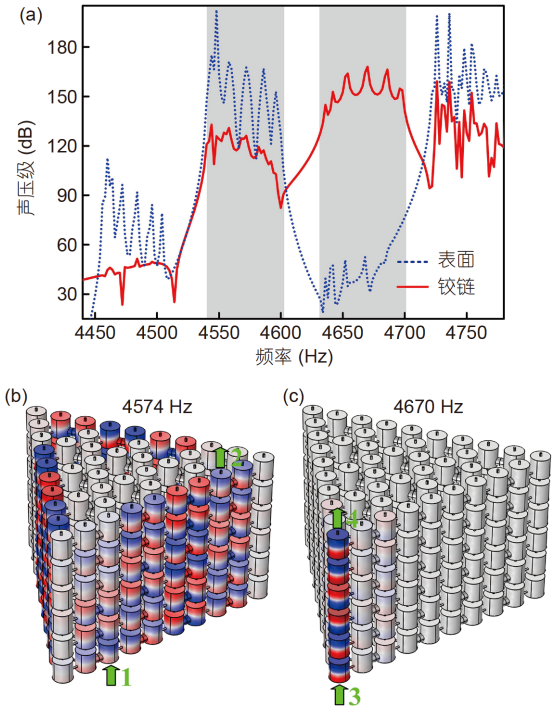


图 6 (网络版彩色)拓扑非平庸型声学超材料的传输效率与声压场分布图. (a) 三维声学超材料的一阶表面态传输曲线(虚线所示)和二阶铰链态传输曲线(实线所示); (b) 频率为4574 Hz的点声源激励下的声压场分布; (c) 频率为4670 Hz的点声源激励下的声压场分布

Figure 6 (Color online) Simulated transmission spectra and acoustic pressure distributions of the topological non-trivial acoustic metamaterials. (a) Simulated transmission spectra of first-order surface states (dotted line) and second-order hinge states (solid line); (b) distribution of acoustic pressure field excited by point acoustic source with frequency 4574 Hz; (c) distribution of acoustic pressure field excited by point acoustic source with frequency 4670 Hz

分布. 结果显示声波能量只集中在声源处, 无法在声学超材料的任何部位传播, 声波传输被完全阻隔. 所以,

平庸型声学超材料的传输效率的计算结果与其超胞能带和特征频率的计算结果拟合较好.

5 总结与展望

本研究提出了一种具有一阶表面态和二阶铰链态的三维声学超材料. 通过调节原胞内部连接管道的直径d_1和外部连接管道的直径d_2, 内耦合强度t_1和外耦合强度t_2的大小被相应改变. 当$d_1=d_2$, 即$t_1=t_2$时, 原胞能带在布里渊区的K-H方向上形成二重简并的交线; 而当$d_1\neq d_2$, 即$t_1\neq t_2$时, K-H方向上的交线被打开, 形成完全带隙. 以此现象为基础设计出两种三维声学超材料: 当$t_1<t_2$时, 超胞能带的完全带隙中具有一阶表面能带和二阶铰链能带, 特征频率中也具有一阶表面特征频率和二阶铰链特征频率, 所以该声学超材料是拓扑非平庸的; 当$t_1>t_2$时, 超胞能带中只具有体能带, 特征频率中也只具有体特征频率, 所以该声学超材料是平庸的. 本研究提出的拓扑非平庸型三维声学超材料实现了声波在三维结构的体、表面和铰链上的调控. 此外, 以基于空气声学提出的三维声学超材料为基础, 借助内外耦合强度的调控, 可以将该研究推广到其他经典波超材料中, 如三维光学高阶拓扑态和三维弹性波高阶拓扑态等. 这类推广可以极大地丰富高阶拓扑态的内容, 对三维结构中光波、声波和弹性波的控制具有重要意义.

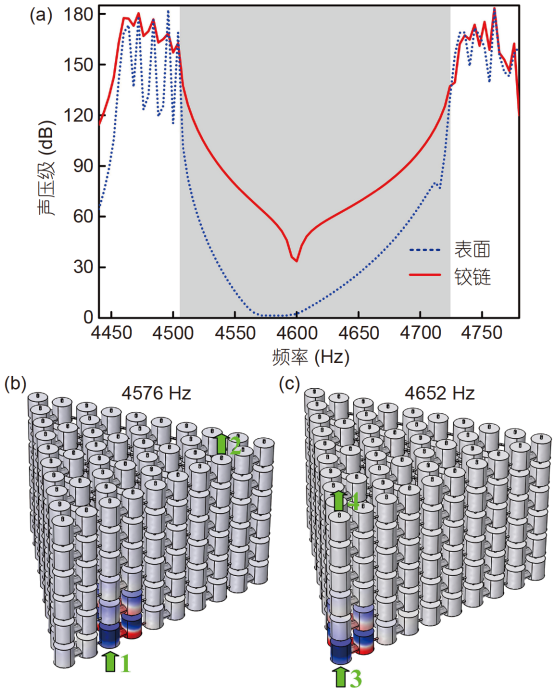


图 7 (网络版彩色)平庸型声学超材料的传输效率与声压场分布图. (a) 三维声学超材料的表面态传输曲线(虚线所示)和铰链态传输曲线(实线所示); (b) 频率为4576 Hz的点声源激励下的声压场分布; (c) 频率为4652 Hz的点声源激励下的声压场分布

Figure 7 (Color online) Simulated transmission spectra and acoustic pressure distributions of the trivial acoustic metamaterials. (a) Simulated transmission spectra of surface states (dotted line) and hinge states (solid line); (b) distribution of acoustic pressure field excited by point acoustic source with frequency 4576 Hz; (c) distribution of acoustic pressure field excited by point acoustic source with frequency 4652 Hz

参考文献

1 He C, Ni X, Ge H, et al. Acoustic topological insulator and robust one-way sound transport. Nat Phys, 2016, 12: 1124–1129
2 Lu J, Qiu C, Ye L, et al. Observation of topological valley transport of sound in sonic crystals. Nat Phys, 2016, 13: 369–374
3 Xue H, Yang Y, Gao F, et al. Acoustic higher-order topological insulator on a kagome lattice. Nat Mater, 2019, 18: 108–112
4 Poo Y, Wu R, Lin Z, et al. Experimental realization of self-guiding unidirectional electromagnetic edge states. Phys Rev Lett, 2011, 106: 093903
5 Xia B, Fan H, Liu T. Topologically protected edge states of phoxonic crystals. Int J Mech Sci, 2019, 155: 197–205
6 Yan M, Lu J, Li F, et al. On-chip valley topological materials for elastic wave manipulation. Nat Mater, 2018, 17: 993–998
7 Li S, Zhao D, Niu H, et al. Observation of elastic topological states in soft materials. Nat Commun, 2018, 9: 1370
8 Xia B, Wang G, Zheng S. Robust edge states of planar phononic crystals beyond high-symmetry points of brillouin zones. J Mech Phys Solids, 2019, 124: 471–488
9 Wang Z, Chong Y, Joannopoulos J D, et al. Observation of unidirectional backscattering-immune topological electromagnetic states. Nature, 2009, 461: 772–775
10 He C, Sun X C, Liu X P, et al. Photonic topological insulator with broken time-reversal symmetry. Proc Natl Acad Sci USA, 2016, 113: 4924–4928
11 Bahari B, Ndao A, Vallini F, et al. Nonreciprocal lasing in topological cavities of arbitrary geometries. Science, 2017, 358: 636–640
12 Fang K, Yu Z, Fan S. Realizing effective magnetic field for photons by controlling the phase of dynamic modulation. Nat Photonics, 2012, 6: 782–787
13 Estep N A, Sounas D L, Soric J, et al. Magnetic-free non-reciprocity and isolation based on parametrically modulated coupled-resonator loops. Nat Phys, 2014, 10: 923–927
14 Cheng X, Jouvaud C, Ni X, et al. Robust reconfigurable electromagnetic pathways within a photonic topological insulator. Nat Mater, 2016, 15: 542–548

15 Ma T, Shvets G. Scattering-free edge states between heterogeneous photonic topological insulators. Phys Rev B, 2017, 95: 165102
16 Xiao B, Lai K, Yu Y, et al. Exciting reflectionless unidirectional edge modes in a reciprocal photonic topological insulator medium. Phys Rev B, 2016, 94: 195427
17 Mittal S, Ganeshan S, Fan J, et al. Measurement of topological invariants in a 2D photonic system. Nat Photonics, 2016, 10: 180–183
18 Parto M, Wittek S, Hodaei H, et al. Edge-mode lasing in 1D topological active arrays. Phys Rev Lett, 2018, 120: 113901
19 Hafezi M, Mittal S, Fan J, et al. Imaging topological edge states in silicon photonics. Nat Photonics, 2013, 7: 1001–1005
20 Nash L M, Kleckner D, Read A, et al. Topological mechanics of gyroscopic metamaterials. Proc Natl Acad Sci USA, 2015, 112: 14495–14500
21 Mitchell N P, Nash L M, Hexner D, et al. Amorphous topological insulators constructed from random point sets. Nat Phys, 2018, 14: 380–385
22 Mitchell N P, Nash L M, Irvine W T M. Realization of a topological phase transition in a gyroscopic lattice. Phys Rev B, 2018, 97: 100302
23 Fleury R, Sounas D L, Sieck C F, et al. Sound isolation and giant linear nonreciprocity in a compact acoustic circulator. Science, 2014, 343: 516–519
24 Khanikaev A B, Fleury R, Mousavi S H, et al. Topologically robust sound propagation in an angular-momentum-biased graphene-like resonator lattice. Nat Commun, 2015, 6: 8260
25 Peng Y G, Qin C Z, Zhao D G, et al. Experimental demonstration of anomalous Floquet topological insulator for sound. Nat Commun, 2016, 7: 13368
26 Wei Q, Tian Y, Zuo S Y, et al. Experimental demonstration of topologically protected efficient sound propagation in an acoustic waveguide network. Phys Rev B, 2017, 95: 094305
27 Fleury R, Khanikaev A B, Alù A. Floquet topological insulators for sound. Nat Commun, 2016, 7: 11744
28 He C, Yu S Y, Ge H, et al. Three-dimensional topological acoustic crystals with pseudospin-valley coupled saddle surface states. Nat Commun, 2018, 9: 4555
29 Slobozhanyuk A, Mousavi S H, Ni X, et al. Three-dimensional all-dielectric photonic topological insulator. Nat Photonics, 2017, 11: 130–136
30 Xiao M, Chen W J, He W Y, et al. Synthetic gauge flux and Weyl points in acoustic systems. Nat Phys, 2015, 11: 920–924
31 Li F, Huang X, Lu J, et al. Weyl points and Fermi arcs in a chiral phononic crystal. Nat Phys, 2017, 14: 30–34
32 Ge H, Ni X, Tian Y, et al. Experimental observation of acoustic Weyl points and topological surface states. Phys Rev Appl, 2018, 10: 014017
33 Benalcazar W A, Bernevig B A, Hughes T L. Quantized electric multipole insulators. Science, 2017, 357: 61–66
34 Ezawa M. Higher-order topological insulators and semimetals on the breathing kagome and pyrochlore lattices. Phys Rev Lett, 2018, 120: 026801
35 Langbehn J, Peng Y, Trifunovic L, et al. Reflection-symmetric second-order topological insulators and superconductors. Phys Rev Lett, 2017, 119: 246401
36 Khalaf E. Higher-order topological insulators and superconductors protected by inversion symmetry. Phys Rev B, 2018, 97: 205136
37 Zhang Z W, Cheng Y, Liu X J. Topological phase transition and edge states in two-dimensional acoustic systems (in Chinese). Physics, 2017, 46: 677–683 [张志旺, 程营, 刘晓峻. 二维声学系统中的拓扑相变及边界传输. 物理, 2017, 46: 677–683]
38 Zheng S J, Xia B Z, Liu T T, et al. Subwavelength topological valley-spin states in the space-coiling acoustic metamaterials (in Chinese). Acta Phys Sin, 2017, 66: 228101 [郑圣洁, 夏百战, 刘亭亭, 等. 空间盘绕型声学超材料的亚波长拓扑谷自旋态. 物理学报, 2017, 66: 228101]
39 Serra-Garcia M, Peri V, Süsstrunk R, et al. Observation of a phononic quadrupole topological insulator. Nature, 2018, 555: 342–345
40 Peterson C W, Benalcazar W A, Hughes T L, et al. A quantized microwave quadrupole insulator with topologically protected corner states. Nature, 2018, 555: 346–350
41 Noh J, Benalcazar W A, Huang S, et al. Topological protection of photonic mid-gap defect modes. Nat Photonics, 2018, 12: 408–415
42 Zhang X, Wang H X, Lin Z K, et al. Second-order topology and multidimensional topological transitions in sonic crystals. Nat Phys, 2019, 15: 582–588
43 Zhang Z, Rosendo López M, Cheng Y, et al. Non-hermitian sonic second-order topological insulator. Phys Rev Lett, 2019, 122: 195501
44 Ni X, Weiner M, Alù A, et al. Observation of higher-order topological acoustic states protected by generalized chiral symmetry. Nat Mater, 2019, 18: 113–120
45 Fan H, Xia B, Tong L, et al. Elastic higher-order topological insulator with topologically protected corner states. Phys Rev Lett, 2019, 122: 204301
46 Su W P, Schrieffer J R, Heeger A J. Solitons in polyacetylene. Phys Rev Lett, 1979, 42: 1698–1701
47 Vanderbilt D, King-Smith R D. Electric polarization as a bulk quantity and its relation to surface charge. Phys Rev B, 1993, 48: 4442–4455

Summary for “三维声学超材料的高阶拓扑态”

Higher-order topological states in a three-dimensional acoustic metamaterial

Haiyan Fan & Baizhan Xia*

State Key Laboratory of Advanced Design and Manufacturing for Vehicle Body, College of Mechanical and Vehicle Engineering, Hunan University, Changsha 410082, China

* Corresponding author, E-mail: xiabz2013@hnu.edu.cn

Topologically gapless edge states, characterized by topological invariants and Berry’s phases of bulk energy bands, provide amazing techniques to robustly control the reflectionless propagation of electrons, photons and phonons. Recently, a new family of topological phases, dictated by the bulk polarization, has been observed, leading to the discovery of the higher-order topological insulators. The higher-order topological states located on the “boundaries of boundaries” can be used to limit and control the transmission of optical waves, acoustic waves and elastic waves. So far, the higher-order topological states have been demonstrated in two-dimensional mechanical, electromagnetic, optical, acoustic and elastic systems. However, the study of higher-order topological states in three-dimensional acoustic systems, which can increase the possibility of topological metamaterial design, is rarely reported. In this letter, we propose a three-dimensional acoustic metamaterial supporting topologically protected second-order hinge states along with topologically protected first-order surface states within the same bandgap.

Only the nearest neighbor couplings are considered in this metamaterial, and the coupling strengths can be adjusted by changing the diameters of the connection pipes. The intra-cell coupling strength t_1 is proportional to the diameters of the intra-cell connection pipes d_1, and the inter-cell coupling strength t_2 is proportional to the diameters of the inter-cell connecting pipes d_2. The band structure of the unit cell of three-dimensional acoustic metamaterial with the same intra-cell and inter-cell coupling strengths can form a two-fold nodal line along the K-H direction of its Brillouin zone. When intra-cell and inter-cell coupling strengths are different, the two-fold nodal line is lifted to form a complete bandgap, yielding two different kinds of acoustic metamaterials, that are, trivial and topological non-trivial metamaterials. The numerical results of band structures and eigenfrequencies indicate that: When the intra-cell coupling strength t_1 is less than the inter-cell coupling strength t_2, the acoustic metamaterial has 3 second-order hinge bands, 12 first-order surface bands and 18 second-order hinge eigenfrequencies, 72 first-order surface eigenfrequencies in the complete bandgap range respectively; when the inter-cell coupling strength t_2 is less than the intra-cell coupling strength t_1, there is neither any energy bands nor any eigenfrequencies in the complete bandgap range. The second-order hinge states and first-order surface states have great immunity against defects, favorably evidencing the strong robustness of the topological states. The numerical results of the transmission spectra furtherly verify the above phenomena. When $t_1<t_2$, the transmission spectrum of the second-order hinge reaches its peak at 4670 Hz. For the first-order surface transmission spectrum, a high peak, located in the bandgap, is observed around 4555 Hz. When $t_1>t_2$, the surface and hinge transmission spectra are very low within the complete bandgap, the acoustic energy is concentrated only at the excitation cylinder, showing that the acoustic wave will not propagate in any part of the acoustic metamaterial in the complete bandgap range and the acoustic metamaterial is trivial. The realization of the higher-order topological states in three-dimensional acoustic metamaterial breaks through the limitation of that in two-dimensional system, realizes the topologically transform of acoustic energy among bulk, surface and hinge states and has the potential application prospect in acoustic energy recovery and high-precision acoustic sensor.

three-dimensional acoustic metamaterial, higher-order topological insulator, topological surface state, topological hinge state, band structure

doi: 10.1360/TB-2019-0631